Journal of Power Sources 558 (2023) 232547

Contents lists available at ScienceDirect

Journal of Power Sources

journal homepage: www.elsevier.com/locate/jpowsour

Lithium-rich antiperovskite (Li_2Fe)SeO: A high-performance cathode material for lithium-ion batteries

M.A.A. Mohamed [a,c,1], L. Singer [b,1], H. Hahn [b], D. Djendjur [b], A. Özkara [b], E. Thauer [b], I.G. Gonzalez-Martinez [a], M. Hantusch [a], B. Büchner [a], S. Hampel [a], R. Klingeler [b,*], N. Gräßler [a,*]

[a] Leibniz Institute for Solid State and Materials Research Dresden e.V., 01069 Dresden, Germany
[b] Kirchhoff Institute for Physics, Heidelberg University, 69120 Heidelberg, Germany
[c] Department of Physics, Faculty of Science, Sohag University, 82524 Sohag, Egypt

HIGHLIGHTS

- Synthesis of antiperovskite (Li_2Fe)SeO using one-step solid-state method.
- Demonstrating its potential as Lithium ion battery cathode material.
- High capacity of ~150 mAh g^{-1}at 0.1 C and high current capability of 100 mAh g^{-1}at 1 C.
- (Li_2Fe)SeO displays outstanding cycling stability and storage per formula unit.

GRAPHICAL ABSTRACT

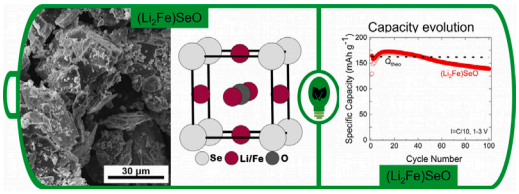

ARTICLE INFO

Keywords:
Antiperovskites
Lithium-ion battery
Lithium-rich cathode material

ABSTRACT

Lithium-rich antiperovskite cathode materials with cationic and anionic redox bi-functionality are promising candidates for lithium-ion batteries (LIB) with high energy density. Here, we report the synthesis of antiperovskite (Li_2Fe)SeO by means of an one-step solid-state method which results in phase pure material consisting of predominantly micrometer-sized particles. Thermodynamic investigations confirm high thermal stability of (Li_2Fe)SeO up to 1200 °C without any indication of phase decomposition. Electrochemical studies of (Li_2Fe)SeO-based cathodes show a multi-step redox process involving electrochemical activity of cationic Fe and anionic Se. Rate capability tests yield a discharge capacity of 150 mAh g^{-1} and 100 mAh g^{-1} at 0.1 C and 1 C, respectively. In-depth kinetic analyses by *in-situ* electrochemical impedance spectroscopy indicate a considerable structural change primarily in the first cycle, however, the structure stabilizes afterwards in the following cycles. Accordingly, we observe superior high cycling stability. Upon cycling, the material displays only a slight capacity fading while still delivering 140 mAh g^{-1}after 100 cycles at 0.1 C. Our findings highlight the high performance and compelling cycling stability of (Li_2Fe)SeO as cathode material in lithium-ion batteries.

1. Introduction

In current commercial cathode materials, maximum capacity is limited to one or less electron transfer per formula unit [1]. The class of lithium-rich cathode materials promises to surpass this barrier as they exhibit multi-electron redox activity [2]. In general, multi-electron charge transfer can be obtained by (i) multi-stage redox processes of transition metal cations or (ii) the coupled redox processes of transition metal cations and anions [1,3]. One class that can exhibit such advantage are Li-rich oxides [2]. However, storing more than one electron per formula unit is difficult to actually implement in materials

* Corresponding authors.
E-mail addresses: klingeler@kip.uni.heidelberg.de (R. Klingeler), n.graessler@ifw-dresden.de (N. Gräßler).
[1] Both authors contributed equally.

https://doi.org/10.1016/j.jpowsour.2022.232547
Received 6 May 2022; Received in revised form 14 November 2022; Accepted 17 December 2022

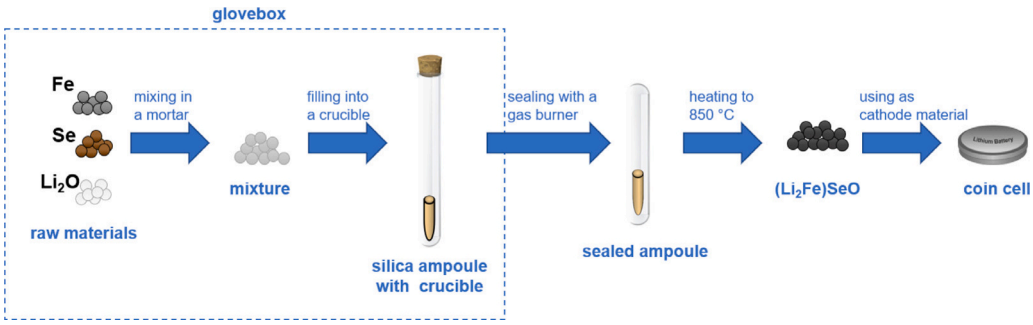

Fig. 1. Schematic diagram of the $(Li_2Fe)SeO$ synthesis.

in practice due to the redox activity of oxygen at high potentials which leads to irreversible O_2 release and decomposition of current commercial electrolytes [4,5]. Therefore, the pursuit of further, more convenient Li-rich cathode materials without such disadvantage is high. Recently, a novel class of Li-rich antiperovskite-structured cathode materials with the general composition $(Li_2TM)ChO$ (TM = Fe, Mn, Co :Ch = S, Se) was reported [6,7]. This class circumvents the problems appearing in Li-rich oxides by the lower redox potentials of the anionic sulfides/selenides [8]. In fact, their reversible multi-electron storage originates from the coupled redox activity of transition metal cation and the sulfide/selenide anion [9]. First measurements on the antiperovskite cathode material $(Li_2Fe)SO$ already proved its promising electrochemical performance by showing discharge capacity of ~285 mAh g^{-1} at 0.1 C and high rate capability (~200 mAh g^{-1} at 1 C) when cycled between 1.2 and 3 V [9]. However up to now only a limited cycling stability of the antiperovskite cathodes was achieved [9]. Some progress was made by the partial anionic substitution of S^{2-} with Se^{2-}, which was found to tune the cycling stability and the working potential in the $(Li_2Fe)S_{1-x}Se_xO$ series (x = 0.1–0.9) [10]. The antiperovskite-structured cathode material $(Li_2Fe)SeO$ was initially electrochemically characterized by Lai et al. [6] by means of a few-cycle experiment using homemade plastic bag batteries (vs. graphite). However, only modest electrochemical properties have been reported, including the initial discharge capacity of ~120 mAh g^{-1} at ~0.18 C and in particular pronounced capacity fading to 98 mAh g^{-1} after only 5 cycles (~18 percent capacity fade) [6].

Here, we report on the actually outstanding performance that $(Li_2Fe)SeO$ can display. We show that $(Li_2Fe)SeO$-based electrodes exhibit an initial specific discharge capacity of 164 mAh g^{-1} at 0.1 C. During cycling the here presented $(Li_2Fe)SeO$ exhibits only a slight capacity loss leading to still ~140 mAh g^{-1}after 100 cycles. Furthermore, even at the rate of 1 C, $(Li_2Fe)SeO$ delivers a reversible capacity of around 100 mAh g^{-1}. These findings highlight the great potential of $(Li_2Fe)SeO$ as a cathode material for LIB, especially in terms of cycling stability, and promotes further work on Se containing antiperovskite cathode materials.

2. Experimental section

2.1. Synthesis

The material $(Li_2Fe)SeO$ was prepared by a solid-state reaction method. For this process, stoichiometric amounts of Li_2O, Fe and Se (Alfa Aesar) were mixed in an Ar-filled glovebox (MBraun, Germany, H_2O and O_2 levels < 1 ppm), and filled in a corundum crucible (Aliaxis, Frialit-Degussit, AL23). The crucible was placed inside a silica ampoule (QSILAG; Quarzschmelze, Ilmenau) and temporarily closed with a rubber stopper. Outside the glovebox, the ampoule was evacuated, filled with Ar to adjust the pressure to 200 mbar, and finally melt-sealed. The sealed ampoule was heated to 850 °C (heating rate: 50 °C/h) in a furnace and held at this temperature for 3 h. Afterwards the ampoule was quenched in water to prevent the formation of other phases such as transition metal oxides and selenides [6]. Finally, the ampoule was opened inside the glovebox and the final product was used for further characterization and measurements. A schematic diagram showing the synthesis procedure is displayed in Fig. 1

2.2. Characterization

X-ray diffraction (XRD) studies were performed using a STADI P diffractometer (STOE) in Debye–Scherrer geometry using Co $K_{\alpha 1}$ radiation (λ = 1.79026 Å) and a Mythen 1K detector (Dectris). The sample was placed into glass capillary inside the glove box and melt-sealed outside in order to prevent any air exposure during the XRD investigations. Inductively coupled plasma optical emission spectroscopy (ICP-OES) (iCAP 6500 Duo View, Fa. Thermo Fisher Scientific GmbH) was used for elemental analysis. Differential thermal analysis (DTA) up to 1200 °C was performed by means of a Setaram DTA92-2400 (alumina container) under helium atmosphere (heating rate: 10 °C/min). Scanning electron microscopy (Nova-NanoSEM 200) coupled with energy dispersive spectroscopy (EDS) was used to investigate the morphology and composition of the compound. X-ray photoelectron spectroscopy (XPS) was performed with a PHI 5600 spectrometer (Physical Electronics) equipped with a hemispherical analyzer with 29.35 eV pass energy for high resolution spectra, using monochromatic Al-K_α radiation (200 W). To prevent any air exposure the sample was transferred in a special transfer chamber. The estimated spot size on the sample is about 0.4 mm. To avoid charging effects, an electron gun is used as a neutralizer. All binding energies refer to the Li 1s peak at 54.0 eV. Transmission Electron Microscopy (TEM) studies were conducted on a FEI Titan 300-80 TEM with third-order spherical aberration correction. The sample was loaded by direct contact onto Cu 300 mesh TEM grids (Agar) and holey carbon film (Plano). High-resolution imaging was performed at 300 kV.

2.3. Electrochemical studies

Electrochemical measurements were carried out using a VMP3 potentiostat (BioLogic) at 25 °C. Slurry preparation as well as cell assembly have been performed in an Argon-filled glovebox with controlled humidity and oxygen concentration. Working electrodes were prepared by mixing the active material 70%wt, carbon black (TIMCAL SUPER C65) 15%wt, and 15%wt polyvinylidene fluoride (PVDF) in dry isopropanol using a Fisherbrand Model 120 before spreading the resulting mixture onto a (Ø = 10 mm) aluminum mesh (thickness 0.125 mm). Afterwards the obtained electrodes were dried over night in vacuum, pressed and dried again. The mass loading ranged between 3 and 4.5 mg cm^{-2}. For assembling the cells, glass fiber (Whatman GF/D, 675 μm thickness) was used as the separator, pure lithium metal foil (Aldrich) as the counter electrode and 1M $LiPF_6$ in a mixture of ethylene carbonate and dimethyl carbonate (1:1 by weight) as electrolyte [11]. Cyclic voltammetry (CV) and galvanostatic cycling measurements

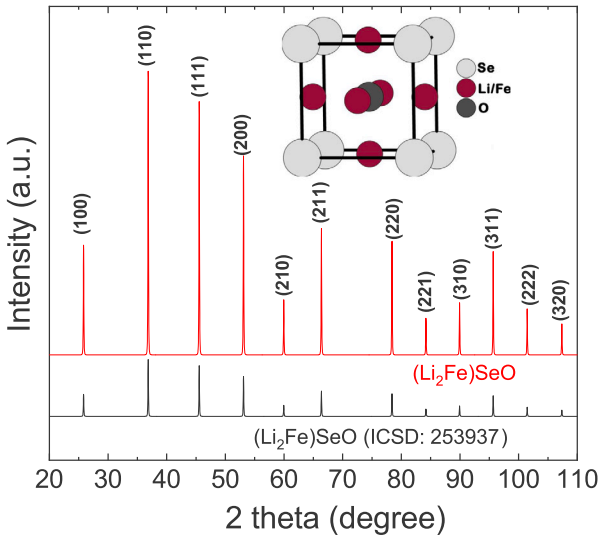

Fig. 2. XRD pattern of $(Li_2Fe)SeO$ (top) with the corresponding reference pattern (ICSD: 253937) [6] and a schematic image of the crystallographic unit cell.

with potential limitation (GCPL) in the voltage range 1 to 3 V were performed in coin cell housing. A 3-electrode PAT-Cell from EL-CELL was used for potentiostatic electrochemical impedance measurements (PEIS). For the PEIS measurements, a small perturbation of 10 mV was applied. In order to ensure the time invariance of the measurement as well as a stable condition, an OVC (open circuit voltage) was performed before each PEIS measurement. Note, the theoretical capacity of $(Li_2Fe)SeO$ for the remove/introduce of 1 Li^+ is 162.8 mAh $g^{-1}$and we attribute the rate 1C to the charge/discharge current required to remove/introduce 1 Li^+ from/into the antiperovskite material within one hour.

3. Results and discussion

Fig. 2 shows the XRD pattern obtained on $(Li_2Fe)SeO$ produced by the solid state reaction method. All diffraction peaks can be identified at the expected Bragg positions for the cubic antiperovskite structure with the *Pm-3m* space group. The XRD pattern does not indicate any additional impurities within its detection limit. The XRD analysis (see Supplemental Information) suggests high crystallinity of the material and shows a large crystallite size combined with a low lattice strain. We obtain the lattice parameter $a = 4.0028(6)$ Å which matches well with the reported value (4.0025 Å) [6].

The ICP-OES analysis of the sample (see Table S1) shows a good agreement of the calculated elemental composition with the nominal composition of the material. Two consecutive cycles of DTA measurements confirm the congruent melting of $(Li_2Fe)SeO$ without indication of intermediate phase decomposition/transition (see Fig. S2). Note, that the absence of additional thermal processes in addition to main melting/crystallization further confirms high purity of the obtained sample. The DTA data imply a melting peak temperature at 1037(2) °C and a crystallization peak at 1008(2) °C. This thermal behavior suggests higher thermal stability of $(Li_2Fe)SeO$ compared to $(Li_2Fe)SO$ [6] and coincides well with the reported thermal trend for the series $(Li_2Fe)S_{1-x}Se_xO$ [10]. The better thermal stability may be attributed to the higher tolerance factor (~0.897) of $(Li_2Fe)SeO$ compared to $(Li_2Fe)SO$ (~0.85) [6,12].

3.1. Physicochemical properties

SEM images of $(Li_2Fe)SeO$ (see Fig. 3(a) and (e)) show that the sample exhibits non-uniform particle shape with large size distribution. The particle size ranges from several tens of micrometers up to submicrometer. Due to the high ionic conductivity of antiperovskites [13], even micrometer-sized $(Li_2Fe)SeO$ particles can be used in actual electrodes for lithium-ion batteries. A large particle size distribution in turn allows for a high tapping density, which is one of the key criteria for a positive industrial outlook [14]. In addition, a homogeneous distribution of Fe, Se and O elements is observed from SEM-EDS mapping images (as seen in Fig. 3 (b–d)), while Li could not be detected by EDS due to its low radiation energy.

High-resolution TEM images (Fig. 4(a) and (b)) provide further insight into the material under study. The images show lattice fringes of the atomic planes of only few crystalline domains. However, the thickness of the shown particle in some areas causes significant overlapping of the lattice fringes of some domains stacked along the optical axis. The average d-spacing for the (110) plane is found to be ~0.301(1) nm which is larger than the expected value from XRD (0.28309(2) nm).

This discrepancy may be attributed to the effect of dislocations and lattice strain on the lattice fringes as observed in the inverse Fourier Transformation FFT in the inset of Fig. 4(a) and (b), which leads to a slight error in the estimation of the d-spacing value from the TEM images. In contrast, the average d-spacing for (210) is found to be close (0.184(7) nm) to the expected XRD value (0.178992(9) nm). Regions with unexpectedly large d-spacings (0.56(3) nm) appeared in a few particles. Such regions may suggest the presence of minor FeSe or $FeSe_{1-x}$ impurities. Due to their characteristic magnetic properties [15], from magnetization data (see Fig. S3 in the Supplemental Information) we infer the presence of small amounts of β−$Fe_{1-x}Se$ with $x \approx 0.25$ ($\lesssim$1 w%) and possibly γ−$Fe_{1-x}Se$ with $x \approx 0.13$. The invisibility of such impurities in the XRD pattern indicates their negligible content.

XPS analyses were performed to investigate the composition and chemical states of the as prepared $(Li_2Fe)SeO$. Fig. S4 shows the full XPS spectrum with clear photoemission peaks for the expected elements. The large background observed at high binding energies is attributed to the increased effect of inelastic photoemission [16]. To get a deeper insight into the oxidation states present, Fig. 5 displays the high resolution spectra of Li 1s, Se 3d and Fe 3p (a) and Fe (b). The similar binding energies of Li 1s, Se 3d and Fe 3p [17] and the observed strong merging of them into only one clearly visible peak (see Fig. 5(a)), impedes a precise quantification of the surface composition. This is especially true since the relative sensitivity factor of Fe 3p is 30 times higher than Li 1s which further complicates the separation process [18]. Nevertheless, the Li 1s peak at 54 eV was adjusted as reference for charge correction which can result in underestimation of the observed binding energies compared to the real ones. The Fe 2p high resolution spectrum (Fig. 5(b)) shows two distinct features due to spin–orbit splitting corresponding to Fe $2p_{3/2}$ and Fe $2p_{1/2}$, respectively [18,19]. The clear appearance of satellite feature for Fe $2p_{1/2}$ combined with multiple splitting of the Fe $2p_{1/2}$ and $2p_{3/2}$ suggests a high-spin state for Fe^{2+} as reported previously for $(Li_2Fe)SO$ based on Moessbauer spectroscopy [9,20]. To further analyze the selenium oxidation state present in our $(Li_2Fe)SeO$ sample, Fig. 5(c) displays the high-resolution Se 3p spectrum. Spin–orbit coupling leads to a splitting of the Se 3p peak into two peaks at 160.12 eV ($3p_{3/2}$) and 165.75 eV ($3p_{1/2}$). The observed binding energies of Se $3p_{3/2}$ and Se $3p_{1/2}$ are close to the values reported for Se^{2-} in other compounds such as CdSe [21] and ZnSe [22]. The slight difference between the here obtained binding energies of Se 3p compared to the values of CdSe and ZnSe can be attributed to the different chemical environment. This finding confirms the existence of Se with oxidation state −2 in $(Li_2Fe)SeO$. Accordingly, the XPS results support the successful formation of $(Li_2Fe)SeO$ with high spin Fe^{2+}.

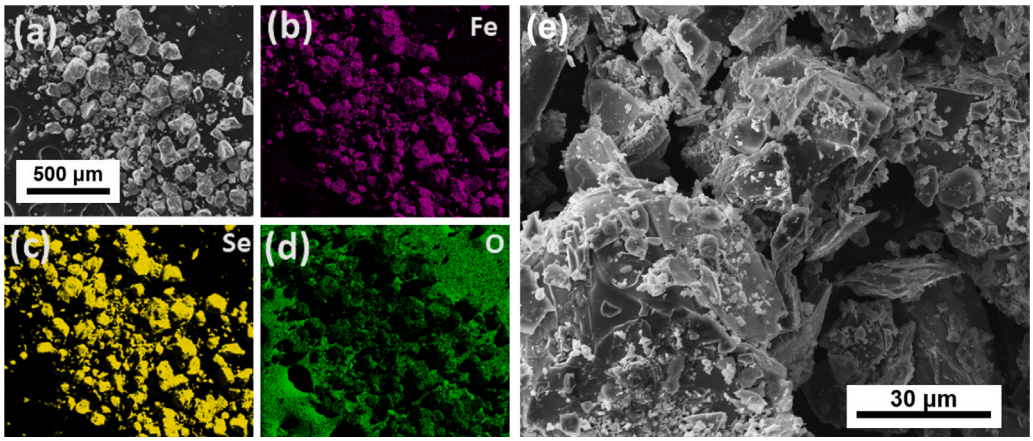

Fig. 3. SEM images of (Li_2Fe)SeO at low (a) and high (e) magnifications as well as (b–d) the EDS-mapping images corresponding to (a).

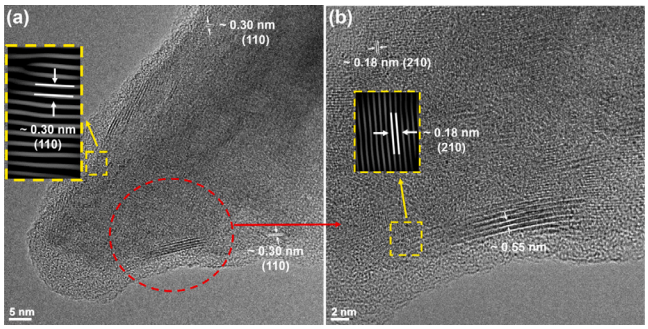

Fig. 4. TEM pictures and analysis of a representative (Li_2Fe)SeO particle. (a) Survey TEM image of one selected (Li_2Fe)SeO particle and (b) enlarged section of the red marked area in (a). The yellow dashed framed insets display the inverse FFT images for specific regions. The *d*-spacing and the corresponding crystal planes are marked in white. (For interpretation of the references to color in this figure legend, the reader is referred to the web version of this article.)

3.2. Electrochemical performance

The electrochemical properties of (Li_2Fe)SeO are investigated with regard to its applicability as an cathode material in LIB. The cyclic voltammograms in Fig. 6 demonstrate that (Li_2Fe)SeO undergoes a multistage Lithium extraction process (see the peaks O1, O2, O*) during the first charge, which shares similarities with the behavior observed in mixed phase (Li_2Fe)$S_{1-x}Se_xO$ [10]. The multistage oxidation behavior observed can be traced back to cationic as well as anionic processes. The first initial oxidation peaks O1 and O2 are typically assigned to the two-stage cationic oxidation process Fe^{2+} to Fe^{3+} [9,10,23]. In a previous report on the related material (Li_2Fe)SO, the high voltage process O* was ascribed to the anionic process ($S^{2-} \rightarrow S^0$) by means of XPS and XAS studies [9]. Up to now this reaction could not be further clarified and the reversibility of the process is also still under discussion. During incorporation of Lithium (discharge), much broader peaks (R1, R2, R3) appear in the cyclic voltammogramms. The main double peak (R1/R2) at ~2 V can be attributed to the reversible reduction of iron. Notably is the much smaller voltage difference between R1/R2 compared to the voltage difference of O1/O2 in the oxidation cycle. In addition, the low voltage region shows a small reduction peak R3 at ~1.5 V and an oxidation peak O3 at 1.7 V. The origin of these peaks remains unclear, even though previous reports on similar compounds (Li_2Fe)SO ($Li_2Fe_{0.9}Mn_{0.1}$)SO, ($Li_2Fe_{0.9}Co_{0.1}$)SO and ($Li_2Fe_{0.5}Mn_{0.5}$)SO have already shown similar low voltage features [10,23,24]. In the following cycles the reduction peaks (R1,R2,R3) and the oxidation peak O3 increase in height without significant broadening. The high voltage oxidation peaks however shift to lower voltages, broaden and decrease in height, which indicates a changing reaction mechanism and a different kinetics between charge and discharge. The hypothesis of a different kinetics during charge/discharge is supported by the GITT measurements on (Li_2Fe)SO [9].

In Fig. 7(a) the superior performance of (Li_2Fe)SeO is shown by a rate capability test. It yields a reversible capacity of 150, 140, 125 and 100 mAh g^{-1}, at currents rates of C/10, C/4, C/2, and C. When the current density is set again to C/10 in cycle 40, the capacity reaches again 150 mAh g^{-1} which proves good reversibility of the (Li_2Fe)SeO-based electrodes. A deeper insight into the underlying processes and their dependence on the charge/discharge rate is provided by the potential curves in Fig. 7(b). The charge curve in cycle 5 recorded at the current rate of C/10 shows that approximately a capacity of 50 mAh g^{-1} is converted within the low voltage process O3 below 2 V while a capacity of 100 mAh g^{-1} is associated with the high voltage processes (above 2 V) O1, O2, and O*. With increasing current, the capacity

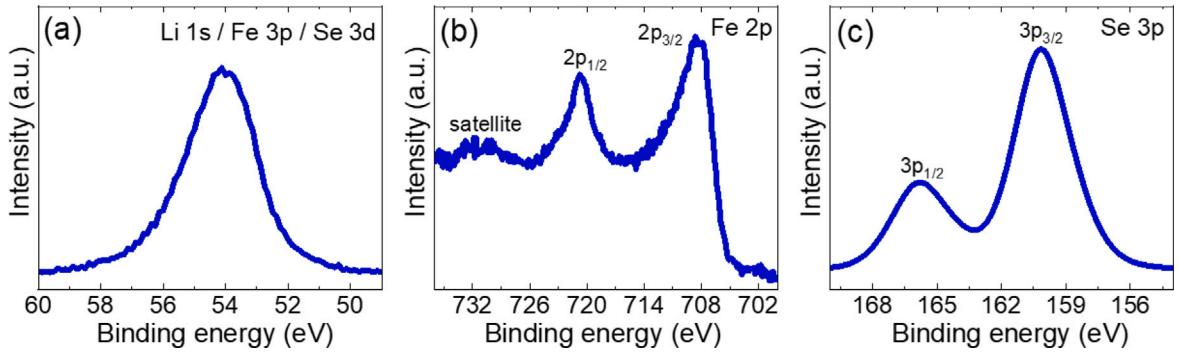

Fig. 5. High-resolution (Li_2Fe)SeO XPS spectra for (a) Li 1s, Se 3d and Fe 3p, (b) Fe 2p and (c) Se 3p.

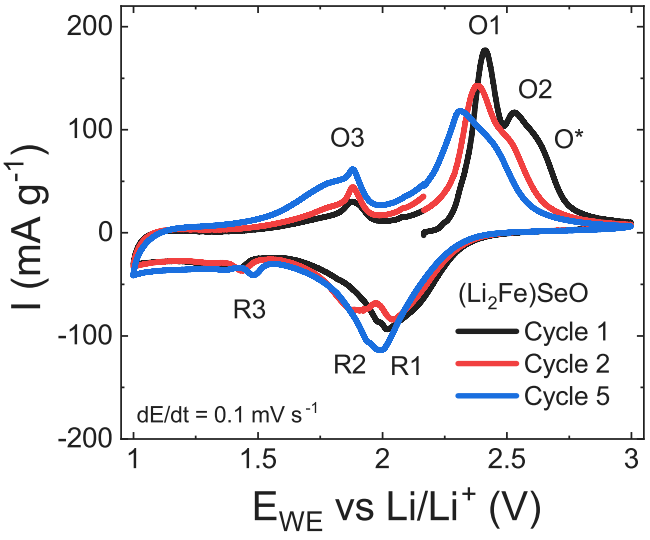

Fig. 6. Cyclic voltammograms of $(Li_2Fe)SeO$ of cycles 1, 2 and 5 recorded at a scan rate of 0.1 $mV s^{-1}$.

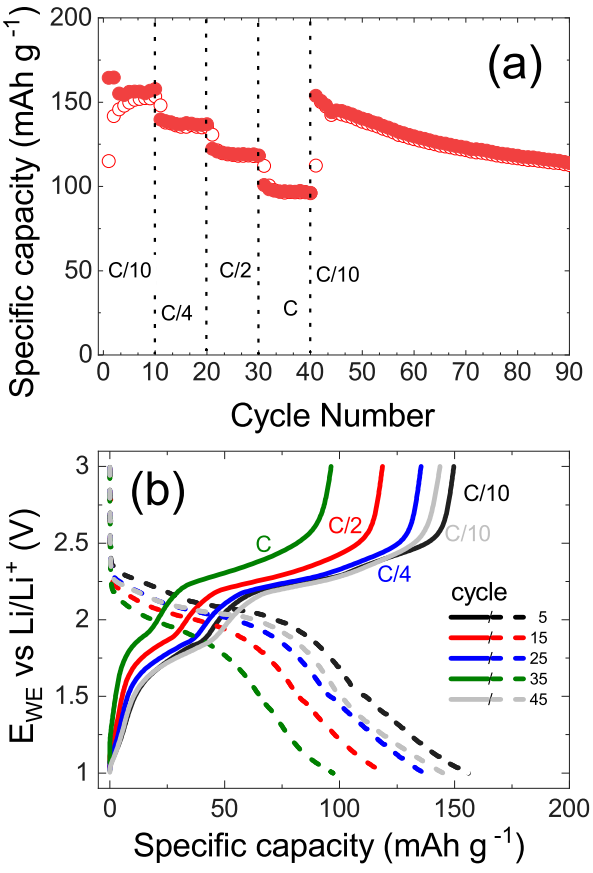

Fig. 7. (a) Evolution of the specific charge/discharge capacities of $(Li_2Fe)SeO$ during rate capability tests with cycling rates between $C/10$ and C and (b) selected corresponding potential profiles of $(Li_2Fe)SeO$. Open/full markers indicate de/lithiation.

associated with the high voltage processes increases (~67% at C/10 to ~79% at 1 C) indicating the high voltage processes to exhibit faster kinetics then the low voltage ones. Returning to a rate of C/10 in cycle 45 results in an increase of the contribution of the low voltage process at the expense of the high voltage one. This observation suggests that

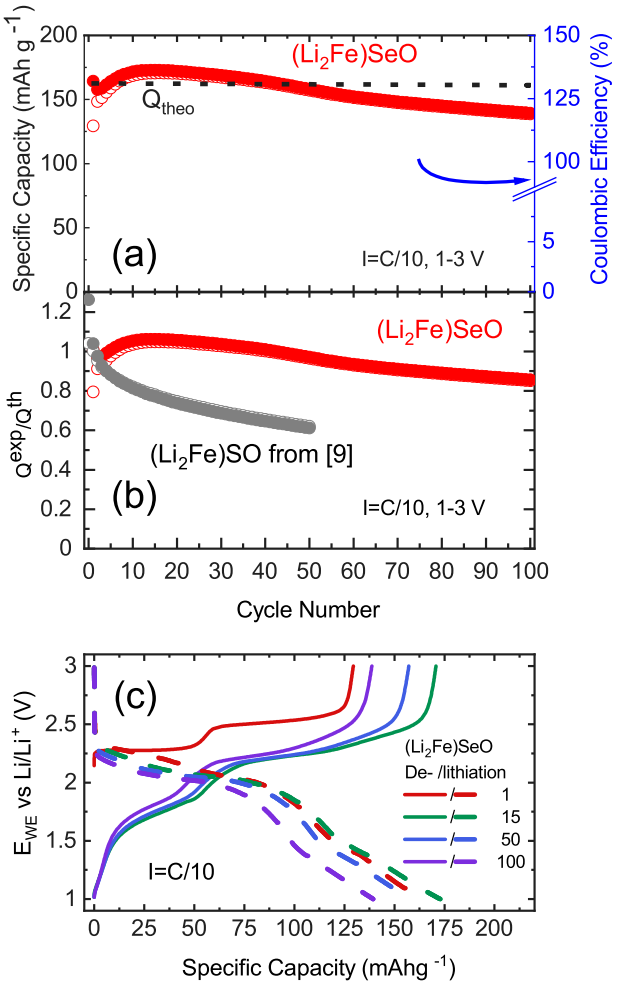

Fig. 8. (a) Specific charge/discharge capacities obtained at C/10 for 100 cycles. (b) Relative specific charge/discharge capacities with respect to the theoretical capacity of one Li insertion/extraction. Grey data markers show results on $(Li_2Fe)SO$ from Ref. [9]. Open/full markers indicate de/lithiation. In (c) selected potential profiles of the $(Li_2Fe)SeO$-electrode are displayed.

the capacity fading is mainly attributed to the high voltage processes O1, O2, and O* as these processes show a regression during cycling.

Long-term galvanostatic cycling performance of $(Li_2Fe)SeO$-cathodes at C/10 is displayed in Fig. 8(a) where dis-/charge capacities are presented. $(Li_2Fe)SeO$ shows an initial charge/discharge capacities of 128/164 mAh g^{-1}. In the next 10 cycles the converted capacity increases to around 170 mAh g^{-1}. Thereafter, a slight monotonous decrease in converted specific capacity to 139 mAh g^{-1} in cycle 100 is observed. The large difference between charge and discharge capacity in the first cycle is also evident in the Coulombic efficiency, which is for the first cycle 126%. Values over 100% strongly point to an irreversible process happening in the first cycle. Afterwards the Coulombic Efficiency decreases to a value slightly above 100% demonstrating the stability of $(Li_2Fe)SeO$.

Fig. 8(b) compares the relative specific capacity (Q experimental/theoretical) of $(Li_2Fe)SeO$ (current study) with the reported $(Li_2Fe)SO$ antiperovskite cathode [9] during removal/insertion of Li into the corresponding structure. Fig. 8(b) reveals that although $(Li_2Fe)SO$ can initially (first five cycles) insert/extract more lithium than $(Li_2Fe)SeO$, $(Li_2Fe)SeO$ is significantly more stable. $(Li_2Fe)SeO$ demonstrates the possibility to reversibly remove/insert 0.85 lithium even after 100 cycles, which is superior to 0.6 found for $(Li_2Fe)SO$ in cycle 50. Consequently, the results show that $(Li_2Fe)SeO$ is a competitive antiperovskite cathode material particularly in terms of cycling

stability and volumetric capacity. The observed higher stability of $(Li_2Fe)SeO$ upon cycling is accompanied by the higher structural stability of $(Li_2Fe)SeO$ compared to $(Li_2Fe)SO$. The intrinsic higher structural stability of selenium containing li-rich antiperovskites is also reinforced by the higher Goldschmidt factor as well as thermal analysis and XRD studies in air [10]

Further insight into charge storage during cycling can be obtained from the potential profiles in Fig. 8(c). The curves show that the increase in the converted capacity in the first 10–15 cycles can be attributed to the low voltage process. The following decrease in the achieved charge capacity from cycles 15 to 50 is ascribed to the decline of the high-voltage anionic selenium reaction. The slight decrease in converted capacity in cycles 50 to 100 is associated with the whole charging regime with however still a dominant loss in the anionic high voltage region. Sulfur-containing lithium-rich antiperovskites display an even higher loss in the high voltage anionic reaction, which is displayed in the CV [24] and potential profiles [23] of sulfur-containing lithium-rich antiperovskite cathodes. The higher electrochemical reactivity of sulfur also explains the initially higher storage per formula unit of $(Li_2Fe)SO$. We therefore attribute the superior cycling stability of Se-containing lithium-rich antiperovskite cathodes to the less pronounced anionic reaction of selenium compared to sulfur in this materials [25]. The conclusion that the sulfur/selenium reaction is of great importance is furthermore supported by studies on $(Li_2Fe)S_{1-x}Se_xO$ [10] which show a shift of the high voltage peak in the reported first cycle CV as a function of selenium content, i.e., the anionic reaction in the first cycle distinctly changes with x. The high-voltage anionic reaction is hence critical for the obtained electrochemical performance. Introducing additional protective coating or the use of different electrolytes could enhance the stability further. A further comparison of our work in terms of electrochemical performance and especially of cycling stability with the recently reported lithium-rich antiperovskites cathodes [10] is not applicable. The here presented galvanostatic study applies a standard protocol as described above which is in contrast to the cycling protocol used in the previous reports [10] where the maximum capacity seems to be limited to a theoretically predicted decomposition value [26]. The latter approach may lead to a severe overestimation of the cycling stability so that comparison of the electrochemical performance from Ref. [10] with our data is not feasible.[2]

To examine the kinetics present in $(Li_2Fe)SeO$ in more detail, potentiostatic electrochemical impedance measurements (PEIS) were carried out at a specific state of charge in different cycles at frequencies between 200 kHz and 5 mHz (see Fig. S5). The corresponding Nyquist plots as well as the fits applied to the data using the Z Fit function of the EC-Lab (Bio-Logic) software are presented in Fig. 9. Qualitative analysis by fitting the data with the corresponding equivalent circuit (see Fig. S6) enables to evaluate the impact of cycling on the electrolyte resistance R_e, on the charge transfer resistance between electrolyte and electrode material R_{ct}, and on the double layer capacitance C_{dl}. The obtained fit parameters are listed in the table S2. After OCV, the Nyquist diagram exhibits a small depressed semicircle in the high to medium frequency range representative for charge transfer followed by a steep rise in the low-frequency range, whose slope is representative for the diffusion impedance of Li^+ ions inside the cathode. Qualitative analysis yields an electrolyte resistance of 2.0(3) Ω, a rather small charge transfer resistance of 15.4(4) Ω and a double layer capacitance of 3.2(3) μF. After one cycle the impedance response of $(Li_2Fe)SeO$ is

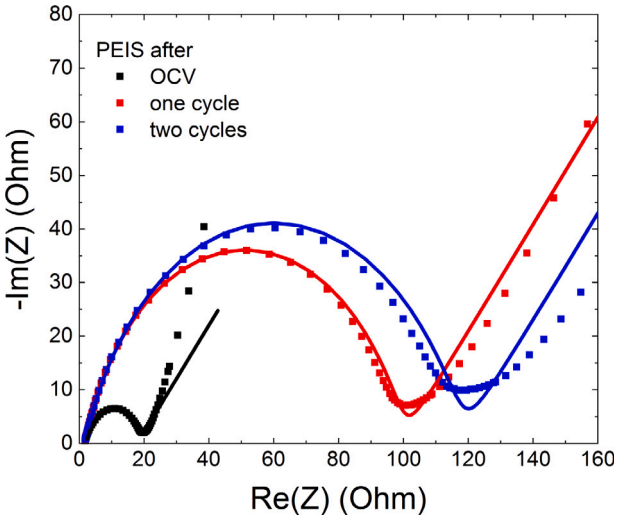

Fig. 9. Nyquist plots for $(Li_2Fe)SeO$ measured at different cycles. Solid lines show fits according to the equivalent circuit used (see the text).

practically unchanged with respect to R_e and C_{dl} while R_{ct} strongly increases to around 98 Ω. This strong increase of R_{ct} implies a major change of $(Li_2Fe)SeO$ in the first cycle. After cycle 2, the PEIS data again confirm quasi unchanged R_e and C_{dl} values and a further, but significantly smaller increase of R_{ct} to ~115 Ω indicating further slight change of $(Li_2Fe)SeO$. Examination of the measured low-frequency impedance response, which reflects the diffusion, reveals a significantly higher slope than the 45-degree slope predicted by the Warburg element. The higher slope of the measured low frequency impedance after OCV indicates that ion diffusion in $(Li_2Fe)SeO$ is likely multi-dimensional [27]. During cycling, a flattering of the slope of the low frequency response during cycling is visible which is indicative for structural change. Again the most significant change occurs within the first cycle. In conclusion, the PEIS Data demonstrated that $(Li_2Fe)SeO$ undergoes strong structural changes during the first cycle and then stabilizes more and more. The observation of structural changes during the first cycle is consistent to data shown in previous reports [9,24].

4. Conclusions

In summary, phase pure $(Li_2Fe)SeO$ was synthesized via a solid-state method with particles in the range of several tens of micrometers up to sub-micrometer in size. A thermally stable behavior with congruent melting is confirmed by differential thermal analysis. Electrochemical characterizations demonstrate a multistage extraction/insertion mechanism of $(Li_2Fe)SeO$ based on cation Fe as well as anion Se activity. Further electrochemical performance test on $(Li_2Fe)SeO$ displayed not only a high current capability of 100 mAh g^{-1} at 1 C but also high cycling stability cooperated by high coulombic efficiency. These promising results persist leading to an overall superior cycling stability and storage per formula unit of $(Li_2Fe)SeO$ compared to its isostructural $(Li_2Fe)SO$. In addition, the electrochemical impedance spectroscopy measurements shed a light onto the kinetics of $(Li_2Fe)SeO$ and the respective changes during cycling. The results displayed major structural change primarily in the first cycle with a strong trend in the next cycle towards more structural stability. The here realized electrochemical performance makes the antiperovskite $(Li_2Fe)SeO$ a competitive cathode material for Lithium ion batteries and nominates Se containing antiperovskites for further optimization and investigations. One attractive option for further improvement involves reduction

[2] Specifically, in our protocol there are no predefined constraints regarding the converted capacity. When limiting the maximum capacity to a defined value, in an initial cycling regime the experimentally obtained capacity values may just reflect the chosen constraint parameters. Even though, the limitation of the capacity may not prevent irreversible processes in general but rather allows them to gradually proceed while the protocol yields seemingly stable capacity values.

of the particle size to shorten the ionic diffusion length inside the bulk cathode, and hence, improve the ionic conductivity for high current rate applications.

CRediT authorship contribution statement

M.A.A. Mohamed: Conceptualization, Experiments, Original draft preparation, Visualization. **L. Singer:** Conceptualization, Experiments, Original draft preparation, Visualization. **H. Hahn:** Experiments. **D. Djendjur:** Experiments. **A. Özkara:** Experiments. **E. Thauer:** Experiments. **I.G. Gonzalez-Martinez:** Experiments. **M. Hantusch:** Experiments. **R. Klingeler:** Conceptualization, Original draft preparation, Visualization, Supervision. **N. Gräßler:** Conceptualization, Original draft preparation, Visualization, Supervision.

Declaration of competing interest

The authors declare that they have no known competing financial interests or personal relationships that could have appeared to influence the work reported in this paper.

Data availability

Data will be made available on request.

Acknowledgments

Financial support by Deutsche Forschungsgemeinschaft (DFG) through project KL 1824/12-1 and by BMBF via the project SpinFun (13XP5088) is acknowledged. Work has also been supported within the framework of the Excellence Strategy of the Federal and State Governments of Germany via Heidelberg University's flagship EMS initiative. M.A.A. Mohamed thanks the IFW excellence program for financial support. N. Gräßler acknowledges funding from the European Regional Development Fund through Sächsische Aufbaubank and project LUKSIAK (Project number 100350438). S. Hampel acknowledges the financial support by the German Research Foundation (DFG) within project VA831/4-1. The authors thank Andrea Voss and Anne Voidel (IFW Dresden) for performing ICP-OES measurements.

Appendix A. Supplementary data

The Supplemental Material presents ICP-OES results, a detailed explanation how d_{XRD} was determined, DTA thermograms, magnetization data, XPS survey spectrum, and further information on PEIS measurements and their analysis.

Supplementary material related to this article can be found online at https://doi.org/10.1016/j.jpowsour.2022.232547.

References

[1] G. Assat, J.-M. Tarascon, Fundamental understanding and practical challenges of anionic redox activity in Li-ion batteries, Nature Energy 3 (5) (2018) 373–386.
[2] W. Zuo, M. Luo, X. Liu, J. Wu, H. Liu, J. Li, M. Winter, R. Fu, W. Yang, Y. Yang, Li-rich cathodes for rechargeable Li-based batteries: reaction mechanisms and advanced characterization techniques, Energy Environ. Sci. 13 (12) (2020) 4450–4497.
[3] C.J. Hansen, J.J. Zak, A.J. Martinolich, J.S. Ko, N.H. Bashian, F. Kaboudvand, A. van der Ven, B.C. Melot, J. Nelson Weker, K.A. See, Multielectron, cation and anion redox in lithium-rich iron sulfide cathodes, J. Am. Chem. Soc. 142 (14) (2020) 6737–6749.
[4] E. McCalla, A.S. Prakash, E. Berg, M. Saubanère, A.M. Abakumov, D. Foix, B. Klobes, M.-T. Sougrati, G. Rousse, F. Lepoivre, S. Mariyappan, M.-L. Doublet, D. Gonbeau, P. Novak, G. van Tendeloo, R.P. Hermann, J.-M. Tarascon, Reversible Li-intercalation through oxygen reactivity in Li-rich Li-Fe-Te oxide materials, J. Electrochem. Soc. 162 (7) (2015) A1341–A1351.
[5] E. McCalla, M.T. Sougrati, G. Rousse, E.J. Berg, A. Abakumov, N. Recham, K. Ramesha, M. Sathiya, R. Dominko, G. van Tendeloo, P. Novák, J.-M. Tarascon, Understanding the roles of anionic redox and oxygen release during electrochemical cycling of lithium-rich layered Li_4FeSbO_6, J. Am. Chem. Soc. 137 (14) (2015) 4804–4814.
[6] K.T. Lai, I. Antonyshyn, Y. Prots, M. Valldor, Anti-perovskite Li-battery cathode materials, J. Am. Chem. Soc. 139 (28) (2017) 9645–9649.
[7] K.T. Lai, I. Antonyshyn, Y. Prots, M. Valldor, Extended chemical flexibility of cubic anti-perovskite lithium battery cathode materials, Inorg. Chem. 57 (21) (2018) 13296–13299.
[8] M. Chen, Y. Liu, Y. Zhang, G. Xing, Y. Tang, Lithium-rich sulfide/selenide cathodes for next-generation lithium-ion batteries: challenges and perspectives, Chem. Commun. 58 (22) (2022) 3591–3600.
[9] D. Mikhailova, L. Giebeler, S. Maletti, S. Oswald, A. Sarapulova, S. Indris, Z. Hu, J. Bednarcik, M. Valldor, Operando studies of antiperovskite lithium battery cathode material $(Li_2Fe)SO$, ACS Appl. Energy Mater. 1 (11) (2018) 6593–6599.
[10] M.A.A. Mohamed, M.V. Gorbunov, M. Valldor, S. Hampel, N. Gräßler, D. Mikhailova, Tuning the electrochemical properties by anionic substitution of Li-rich antiperovskite $(Li_2Fe)S_{1-x}Se_xO$ cathodes for Li-ion batteries, J. Mater. Chem. A 9 (40) (2021) 23095–23105.
[11] G.S. Zakharova, L. Singer, Z.A. Fattakhova, S. Wegener, E. Thauer, Q. Zhu, E.V. Shalaeva, R. Klingeler, MoO_2/C composites prepared by tartaric acid and glucose-assisted sol-gel processes as anode materials for lithium-ion batteries, J. Alloys Compd. 863 (2021) 158353.
[12] H. Zhong, C. Feng, H. Wang, D. Han, G. Yu, W. Xiong, Y. Li, M. Yang, G. Tang, S. Yuan, Structure-composition-property relationships in antiperovskite nitrides: Guiding a rational alloy design, ACS Appl. Mater. Interfaces 13 (41) (2021) 48516–48524.
[13] Z. Deng, D. Ni, D. Chen, Y. Bian, S. Li, Z. Wang, Y. Zhao, Anti–perovskite materials for energy storage batteries, 2021, InfoMat.
[14] R. Jain, A.S. Lakhnot, K. Bhimani, S. Sharma, V. Mahajani, R.A. Panchal, M. Kamble, F. Han, C. Wang, N. Koratkar, Nanostructuring versus microstructuring in battery electrodes, Nat. Rev. Mater. 7 (9) (2022) 736–746.
[15] P. Terzieff, K.L. Komarek, The antiferromagnetic and ferrimagnetic properties of iron selenides with NiAs-type structure, Monatsh. Chem. 109 (5) (1978) 1037–1047.
[16] B. Spencer, S. Maniyarasu, B. Reed, D. Cant, R. Ahumada-Lazo, A. Thomas, C. Muryn, M. Maschek, S. Eriksson, T. Wiell, et al., Inelastic background modelling applied to hard X-ray photoelectron spectroscopy of deeply buried layers: A comparison of synchrotron and lab-based (9.25 keV) measurements, Appl. Surf. Sci. 541 (2021) 148635.
[17] J. Chastain, J.F. Moulder, W.F. Stickle, P.E. Sobol, K.D. Bomben, R.C. King Jr., Handbook of X-ray Photoelectron Spectroscopy: A Reference Book of Standard Spectra for Identification and Interpretation of XPS Data, Physical Electronics, Eden Prairie, Minn., 1995.
[18] R. Dedryvere, M. Maccario, L. Croguennec, F. Le Cras, C. Delmas, D. Gonbeau, X-ray photoelectron spectroscopy investigations of carbon-coated Li_xFePO_4 materials, Chem. Mater. 20 (22) (2008) 7164–7170.
[19] S. Lu, H. Wu, S. Xu, Y. Wang, J. Zhao, Y. Li, A.M. Abdelkader, J. Li, W. Wang, K. Xi, et al., Iron selenide microcapsules as universal conversion-typed anodes for alkali metal-ion batteries, Small 17 (8) (2021) 2005745.
[20] A. Grosvenor, B. Kobe, M. Biesinger, N. McIntyre, Investigation of multiplet splitting of Fe 2p XPS spectra and bonding in iron compounds, Surf. Interface Anal. 36 (12) (2004) 1564–1574.
[21] R. Ospina, S.A. Rincón-Ortiz, J. Rodriguez-Pereira, Cadmium selenide by XPS, Surf. Sci. Spectra 27 (1) (2020) 014021.
[22] J.R. Shallenberger, N. Hellgren, Zinc selenide analyzed by XPS, Surf. Sci. Spectra 27 (1) (2020) 014020.
[23] M.V. Gorbunov, S. Carrocci, S. Maletti, M. Valldor, T. Doert, S. Hampel, I.G. Gonzalez Martinez, D. Mikhailova, N. Gräßler, Synthesis of $(Li_2Fe_{1-y}Mn_y)$so antiperovskites with comprehensive investigations of $(Li_2Fe_{0.5}Mn_{0.5})SO$ as cathode in Li-ion batteries, Inorg. Chem. 59 (21) (2020) 15626–15635.
[24] M.V. Gorbunov, S. Carocci, I.G. Gonzalez Martinez, V. Baran, D. Mikhailova, Studies of $Li_2Fe_{0.9}M_{0.1}SO$ antiperovskite materials for lithium-ion batteries: The role of partial Fe^{2+} to M^{2+} substitution, Front. Energy Res. 9 (2021) 360.
[25] A. Eftekhari, The rise of lithium–selenium batteries, Sustain. Energy Fuels 1 (1) (2017) 14–29.
[26] Z. Lu, F. Ciucci, Anti-perovskite cathodes for lithium batteries, J. Mater. Chem. A 6 (12) (2018) 5185–5192.
[27] X. Zhang, X. Zhang, X. Sun, Y. An, S. Song, C. Li, K. Wang, F. Su, C.-M. Chen, F. Liu, Z.-S. Wu, Y. Ma, Electrochemical impedance spectroscopy study of lithium-ion capacitors: Modeling and capacity fading mechanism, J. Power Sources 488 (2021) 229454.